

3D-printed, electrically conductive structures for magnetic attitude control[☆]

Bonar Robb^{*}, Malcolm McRobb¹, Gilles Baille^t, Colin R. McInnes

James Watt School of Engineering, James Watt (South) Building, University of Glasgow, Glasgow, Scotland, G12 8QQ, United Kingdom

ARTICLE INFO

Keywords:

Attitude control
Large space structures
Gossamer spacecraft
Current loops
Magnetic attitude control
Spring–mass model
Multi-particle model
Spacecraft dynamics and control

ABSTRACT

The use of embedded current loops for the attitude control of large, flexible spacecraft is investigated. Length-scaling laws are derived by determining what fraction of a planar spacecraft's mass would need to be allocated to the conductive current loops in order to produce a torque at least as large as the gravity gradient torque. Simulations are then performed of a flexible truss structure, modelled as a spring–mass system, for a range of structural flexibilities and a variety of current loop geometries. Simulations demonstrate rotation of the structure via the electromagnetic force on the current carrying elements, and are also used to characterise the structural deformations caused by the various current loop geometries. An attitude control simulation is performed, demonstrating a 90° slew manoeuvre of a 250 × 250 m flexible structure through the use of three orthogonal sets of current loops embedded within the spacecraft.

1. Introduction

Large Space Structures (LSS) could be constructed to serve a variety of purposes, both in Earth-orbit (space-based solar power, orbiting solar reflectors, telescopes) and beyond (solar sailing, parabolic reflectors for interplanetary missions, sun-shields). The design and operation of such structures poses a number of engineering challenges. One such challenge is in attitude control, a topic which has received considerable attention with many different strategies proposed. In this paper, we investigate the use of large current loops for the attitude control of LSS. Current loops, i.e. magnetorquers, are widely used for the attitude control of small satellites [1], though this strategy is not often suitable for large spacecraft due to the relatively small torques produced. For some LSS however, particularly those with a low areal density such as membrane or gossamer spacecraft, magnetic control could be a viable form of attitude control [2–4]. Magnetic attitude control in general is attractive due its low cost, power requirements, and its relative simplicity and robustness [5]. With these benefits in mind, this paper aims to address the lack of knowledge surrounding the use of magnetic attitude control via large current loops for LSS. In particular we aim to explore the LSS design space at which the strategy could be most feasible by considering how length-scale, structural flexibility and areal mass density affect the utility of the concept.

Many future LSS are likely to be manufactured on-orbit using additive manufacturing techniques, a paradigm shift from the current

convention of deployable structures which must be stowed during launch and then deployed once in space [6]. On-orbit manufacturing offers a number of advantages over deployables, foremost being that printed structures can be much lighter than a deployable of equivalent scale [7]. This is because the structure does not need to withstand launch loads, and instead needs only be designed to withstand the more gentle disturbing or control forces of its in-space operating environment. Magnetic attitude control could be particularly well-suited to LSS which are 3D-printed on-orbit for the following two reasons. Firstly, as these structures will be extremely lightweight, the relatively small control torques produced by the current loops will be capable of meeting the pointing requirements of LSS of a length-scale greater than would be otherwise possible for conventional constructions. Secondly, as the actuator is simply a loop of conductive material, it would be relatively straightforward to integrate construction of the attitude control system alongside the 3D printing of the main structure. Potential strategies for achieving this could include the direct printing of conductive material, such as through fused metal deposition, or a conductive wire could be embedded within/affixed to the (non-conductive) support structure as it is being 3D-printed. Additive manufacturing of the structure in this fashion would allow the current loops to have complex geometries, capable of producing control torques around multiple axes, a topic which is investigated in Section 2 of this paper.

[☆] An earlier version of this paper was presented at the AIAA Scitech 2020 Forum - “Magnetic Attitude Control of Gossamer Spacecraft using a 3D-printed, Electrically Conducting Support Structure” AIAA 2020-0714.

^{*} Corresponding author.

E-mail addresses: b.rob主.1@research.gla.ac.uk (B. Robb), Gilles.Baille@glasgow.ac.uk (G. Baille), Colin.McInnes@glasgow.ac.uk (C.R. McInnes).

¹ Currently with Mangata Networks.

Magnetic attitude control of LSS has received some attention in the literature. Recent work [2] considered the use of arrays of magnetorquer rods for the attitude control of 75×75 m flexible, planar structures, demonstrating that distributed arrays offered significant advantages over central torquing strategies, and demonstrating de-tumbling and slew manoeuvres in the presence of gravity gradient torques and a time-varying magnetic field. In this paper we consider the quite different problem of large integrated “current loops” as opposed to discrete magnetorquers. A key difference is that magnetic torque rods are generally comprised of wire coiled around a core material with high relative permeability, increasing the field strength and thus torque produced, whereas current loops can be considered to be “air-core” magnetorquers. This distinction is relevant because although both current loops and magnetorquers generate a torque via interaction between a produced and external field, for magnetorquers this torque is increased by having a larger number of turns of the wire and by the core material, both of which increase the mass of the package. For a large current loop embedded in an LSS, a large torque is attained by virtue of the large area enclosed by the current loop. This results in a difference in how these actuators scale with the size of the spacecraft, a subject which we discuss further in Section 3. An early example of a current loop being used for attitude control of a LSS is found in Ref. [3], in which a conceptual design for a 1500 m diameter radiotelescope is presented. Ref. [3] proposes the use of a large current loop around the perimeter of the disk-like telescope structure. When a current is applied to this loop a torque is produced which is used to precess the spin-axis of the rotating telescope, enabling the telescope to scan the celestial sphere. Ref. [8] investigates the use of four current loops for the attitude control of a 15×15 m spinning membrane spacecraft, performing numerical simulations with the membrane modelled as a multi-particle system. These simulations demonstrate precession of the spin-axis by 20° to a target orientation for a variety of cases (different orbits and spin-rates). Similar to Ref. [3], Ref. [8] use the current loop torque to precess the spin axis of a spin-stabilised spacecraft, though Ref. [8] is based on an earlier concept study which demonstrates slew manoeuvres of a non-spinning membrane spacecraft with a perimetric current loop [9]. Also notable is that in these examples the current loops lie in the plane of the spacecraft, and so a torque can only be produced around one axis, while in this paper we consider multiple, orthogonal current loop geometries which could allow the torque direction to be controlled.

A related but distinct concept is the use of current loops for the deployment or tensioning of membrane spacecraft [10–12]. Ref. [10] investigates the use of superconducting current loops to deploy and tension solar sails with radii in the range of 5 to 150 m. A key difference between this concept and our proposed attitude control strategy is that the forces acting on the superconducting loop in Ref. [10] are due to self-interaction of the wire with its own generated magnetic field, whereas we consider current loops interacting with the external geomagnetic field. Generation of these self-forces requires much larger loop currents (on the order of 10^4 A for a 10 m solar sail in Ref. [10]) than are found to be necessary for attitude control purposes, hence the need for superconducting materials in Refs. [10–12].

This paper therefore investigates the feasibility of using large integrated current loops for the attitude control of large space structures. In Section 2, the principles of torque generation via current loops is discussed and a number of candidate current loop geometries for planar structures are presented. Section 3 investigates the maximum length scale of spacecraft that the strategy could be suitable for, by considering a simplified thermal model and relating the torque generated by an embedded current loop of a planar structure to the gravity gradient torque such a structure would experience. In Section 4, results of simulations of a flexible structure with embedded current loops are presented for a range of structural flexibilities and for each current loop geometry. These simulations are used to assess whether current loops are a viable attitude control strategy for ultra lightweight, flexible

structures such as gossamer spacecraft. Finally in Section 5, attitude control of an orbiting 250 m square flexible structure with embedded current loops is demonstrated using a quaternion error feedback control law, in the presence of gravity gradient torques and a representative magnetic field model.

2. Current loop geometries for planar spacecraft

A current loop in a uniform external magnetic field experiences no net force, but will experience a torque which is proportional to the area enclosed by the loop, and the current flowing. The torque arises due to the Lorentz force on the moving charges within the conductive loop, and is given by:

$$\mathbf{T} = I \mathbf{A}_e \times \mathbf{B} \quad (1)$$

where I is the current in the loop, \mathbf{A}_e a vector with magnitude equal to the area enclosed by the loop and normal to that area, and \mathbf{B} the magnetic field vector. The product $I \mathbf{A}_e$ is often referred to as the magnetic dipole moment, \mathbf{m}_d , which characterises the strength of a magnetorquer. Considering a planar, 3D-printed spacecraft with conducting pathways, there are a number of possibilities for the geometries that these current loops could take. The most straightforward geometry is to have one large current loop around the perimeter of the spacecraft (as in Ref. [3]). This current loop would enclose the maximum possible area on the spacecraft, and could only produce attitude control torques around some axis lying in the plane of the structure, due to the cross product in Eq. (1).

The most efficient geometry in terms of the mass required would be a large closed loop, since the maximum area enclosed for a given perimeter length is given by a circle. This geometry is illustrated in Fig. 1A, where the current loop is shown as a blue path on the perimeter of the top layer of the structure. Although less efficient in terms of the path length to enclosed area ratio, for a flexible structure it may be desirable to have multiple current loops spaced throughout the structure, illustrated in Fig. 1B. This geometry would distribute the control torques throughout the flexible structure, which has previously been shown to reduce structural deformations during slew manoeuvres [2]. Fig. 1B shows three current loops on both the top and bottom layer of the structure, though an arbitrary number of loops could be fabricated depending on the flexibility of the structure and thus the need to distribute control torques. A given current loop can only produce torques around one axis, defined by the cross product of the enclosed area surface normal vector and the magnetic field vector in Eq. (1). Magnetic attitude control systems generally employ three orthogonal magnetorquers, so that by varying the current in each torquer control torques can be produced around any axis lying in the plane normal to the field vector. Similarly, this could be achieved for a 3D-printed conductive structure by constructing current loops which enclose area in the yz or xz plane of Fig. 1. Although we are considering a planar structure, these current loops would require the structure to have some depth. One possible configuration is shown in Fig. 1C, which shows current loops lying in the yz plane on each layer of the structure. Another possible configuration is shown in Fig. 1D and detailed in Fig. 1E. In this case, the conducting pathway is formed of a single continuous circuit, rather than separate loops, which winds back and forth across the structure, as shown for a single unit in Fig. 1E. Though this geometry may be less mass efficient than the multiple current loops of Fig. 1D, it may be desirable to have a single continuous pathway, and furthermore this geometry is included as it demonstrates a path geometry that could be implemented in long trusses as well as the planar lattice structure shown here. Fig. 1F shows how three orthogonal coil directions can be achieved by overlaying patterns B and D, where the third direction is achieved by rotating the pattern shown in Fig. 1D by 90° , shown in green on the figure. By varying the current in each loop, the strength and direction of the overall magnetic dipole moment of the system can be specified, allowing torques to be produced in any direction perpendicular to the magnetic field.

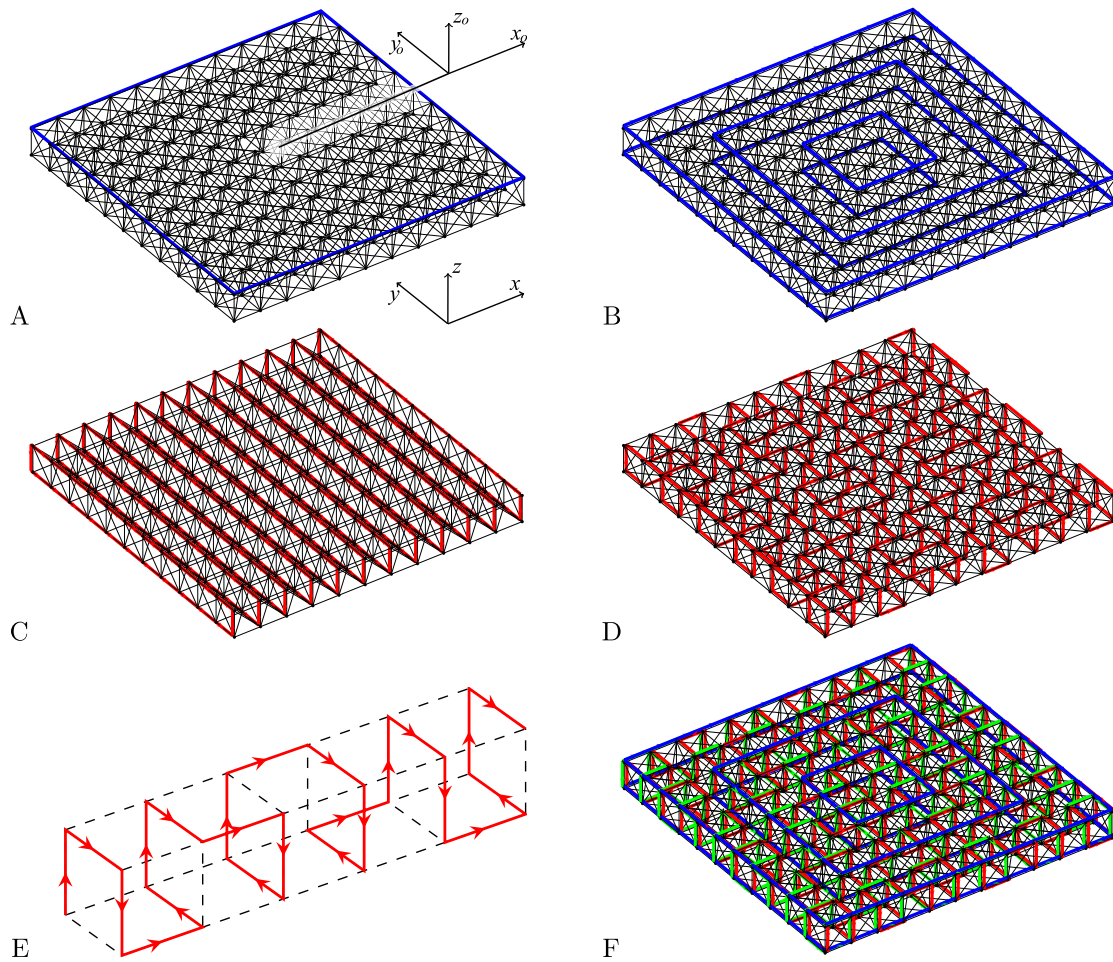


Fig. 1. Current loop geometries for attitude control of a square, planar truss structure. (For interpretation of the references to colour in this figure legend, the reader is referred to the web version of this article.)

3. Length scaling of large current loops

In this section, analysis is undertaken to determine how the effectiveness of the proposed attitude control strategy changes with the length-scale of the spacecraft structure. For this analysis we assume the spacecraft is a homogeneous, square planar structure which has been 3D-printed on-orbit. We assume that during manufacturing, conductive pathways have been embedded in the structure which form closed current loops. We also assume that the conductive pathway itself is a solid, cylindrical wire, and that the spacecraft is orbiting the Earth, where the Earth’s magnetic field is approximated as a dipole field.

The torque generated by the conducting structure is proportional to the current flowing through the conducting pathway. The maximum current depends upon the power available, but will also be limited by the temperature rise in the conductor allowed by the materials of the supporting structure and heat flow between the conductor and support structure. For the analysis of this section, a simplified thermal model of the conductive structure is considered to estimate the extent to which a maximum wire temperature will limit the achievable torque. Fig. 2 illustrates a single unit cube of a conducting structure, consisting of 3D-printed booms or trusses onto which a conducting wire is anchored by thermally insulated nodes attached to the main structure. With a current applied, the power loss due to resistive heating in the wire is given by:

$$P_j = I^2 R \tag{2}$$

for current I and resistance R . The resistance is assumed to vary linearly with temperature over the operational temperature ranges, and

is given by:

$$R = R_r [1 + \alpha(\Gamma - \Gamma_r)] \tag{3}$$

where R_r is the resistance at reference temperature Γ_r , α is the temperature coefficient and Γ the current temperature of the conductor. R_r is inversely proportional to the cross sectional area of the wire, which is assumed to be circular:

$$R_r = \frac{4\rho_r l}{\pi d^2} \tag{4}$$

where ρ_r is the resistivity of the conducting material at the reference temperature, l is the total length of the conductor and d the wire diameter.

Heat leaves the wire through thermal radiation only, as it is assumed that the anchor points are thermally insulating so any heat flow into the support structure is negligible. It is also assumed that a thin film membrane shields the wire from any incoming radiation, as the membrane side of the spacecraft would be directed towards the sun during operation if the spacecraft were acting as a reflector or solar sail. The effect of heat being reflected by the back of the membrane and reabsorbed by the wire is also not considered. It is assumed that the wire is a grey body with emissivity ϵ , so that the power dissipated through thermal radiation is given by the Stefan–Boltzmann law:

$$P_r = \epsilon \sigma A_s \Gamma^4 = \epsilon \sigma \pi d l \Gamma^4 \tag{5}$$

where $\sigma = 5.670373 \times 10^{-8} \text{ W m}^{-2} \text{ K}^{-4}$ is the Stefan–Boltzmann constant, and A_s the surface area of the wire. Of note is that both the resistive heating and thermal radiation are proportional to the length of the

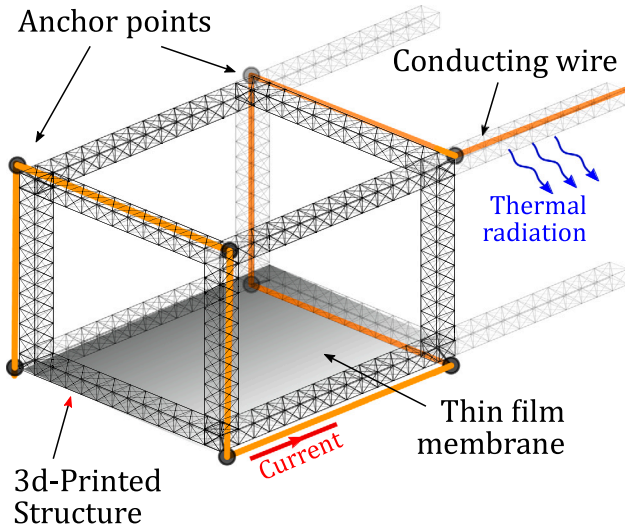


Fig. 2. A unit cube of an implementation of the concept, consisting of a conducting wire anchored to lightweight 3D-printed structural members.

conducting wire, and so the heat flow can be considered per unit length of the conductive path, with units of Watts per meter.

The wire will rise to the temperature at which the resistive heating and thermal radiation are in equilibrium. For a given diameter of wire, there will be a maximum allowable temperature in the conductor depending on the specific construction of the spacecraft. This temperature then determines the maximum current that can be applied to the wire and thus the maximum achievable torque. If the wire were perfectly insulated from the supporting structure, this temperature could be very high, approaching the melting point of the conductor. In practice, it may be desirable to restrict the maximum temperature of the conductor to be below the melting point of the support structure, in case of accidental contact or because there will be radiative heat transfer from the wire to the structure. This restriction would also allow the anchor points to be constructed from the same material as the support structure in a continuous 3D print. Potential materials for 3D-printing the support structure are thermoplastics which could be printed through fused deposition modelling (FDM). We consider polycarbonate as a candidate material for such structures [13], which has a glass transition temperature of around 147°, and a melting point of 155 °C.

Equating P_j and P_r (Eqs. (2) and (5) respectively) allows an expression for d to be found, in terms of I and Γ_e for a given wire material, such that:

$$\epsilon \sigma \pi d \Gamma_e^4 = \frac{4 \rho_r}{\pi d^2} [1 + \alpha(\Gamma_e - \Gamma_r)] \quad (6)$$

where Eq. (3) for R has been substituted into Eq. (2). Therefore, Eq. (6) gives an expression for the wire diameter required to carry a specified current while maintaining thermal equilibrium at the desired temperature. The torque produced is proportional to the current in the conductive path, and to the magnetic field strength which will vary with orbital altitude and position. To proceed we approximate the Earth's magnetic field as a dipole field and consider at a point above the equator, where the field strength is the weakest for a given altitude and thus gives a conservative estimate of the field strength. The field strength is given by [14]:

$$B = B_0 \left(\frac{R_E}{R_o} \right)^3 \quad (7)$$

where $B_0 = 3.12 \times 10^{-5}$ T is the typical field strength on the Earth's surface at the equator, $R_E = 6370$ km is the mean radius of the Earth, and R_o is the orbital altitude. The attitude control torque requirements

for structures with different length scales will vary greatly, due to the scaling of the mass moment of inertia and the scaling of various disturbance torques that will need to be counteracted by the attitude control system. Furthermore, these factors will all vary with altitude as well. We assume that the torque produced by a current loop may be considered “useful” if, for a given length-scale, the torque produced by the current loop has a magnitude at least as great as the maximum gravity gradient torque that the spacecraft will experience, following the discussion in Ref. [2]. The maximum gravity gradient torque for a square, planar structure occurs when the face of the structure is oriented at 45° to nadir, and is given by:

$$T_g^{\max} = \frac{D^2 M \mu}{8 R_o^3} \quad (8)$$

where D is the side-length of the square spacecraft, M the total mass, and $\mu = 3.986 \times 10^{14}$ m³ s⁻² the standard gravitational parameter of Earth. Eq. (8) is found by evaluating the standard gravity gradient torque equation, $T_g = 3\mu/R_o^5(\mathbf{R}_o \times \mathbf{i} \mathbf{R}_o)$ [15], for a square structure which has an inertia tensor i with principal components given by $i_1 = i_2 = \frac{1}{12} M D^2$, $i_3 = 2i_1$, i.e. a square plate with uniform mass density. The subscripts 1, 2 and 3 refer to the x_o, y_o, z_o body frame axes respectively, which is fixed to the structure as shown in Fig. 1.

The torque produced by a current loop depends on the enclosed area, while the mass of that current loops depends on its length. Expressions for both enclosed area and path length as a function of structural side-length are now found. For geometry A of Fig. 1, the enclosed area is given by $A_e = D^2$ for side-length D , and the path length is given by $l = 4D$. For geometries B and C, a general expression is found for N equally spaced loops, while for geometry D the expression is given for N “layers” of coils arranged lengthways across the structure. Additionally, for geometries C and D, the enclosed area of the coils depends on the depth of the structure, w , which is taken to be D/N . Of note is that the following analysis is only accurate for sufficiently large N that $w \ll D$, as it was assumed in Eq. (8) that the structure's inertia tensor is that of a thin square plate. The expressions for A_e and l for the coil geometries considered are summarised in Table 1. For the geometries which contain multiple current loops the number of coils/layers is denoted N , and it is assumed the loops are equally spaced. For the last two geometries, it is further assumed that the depth of the structure is given by D/N , i.e. that the structure can be considered to be composed of square unit cells.

The maximum torque produced by the current loop is $T_L^{\max} = I A_e B$, from Eq. (1). Equating this with the maximum gravity gradient torque (Eq. (8)), which is taken as the reference requirement for useful attitude control, and substituting the dipole field magnitude from Eq. (7) allows an expression for the current required of a current loop to counteract the gravity gradient torque:

$$I A_e B_0 R_E^3 = \frac{D^2 M \mu}{8} \quad (9)$$

We define the conductor mass fraction $\lambda_f = M_c/M$ as the conductor mass divided by the total mass, and express the total mass in terms of the areal mass density σ_A , giving:

$$M = \frac{M_c}{\lambda_f} = \frac{\frac{1}{4} \pi d^2 l}{\lambda_f} = \sigma_A D^2 \quad (10)$$

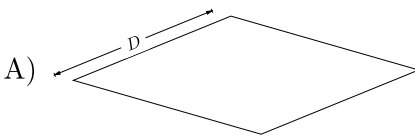
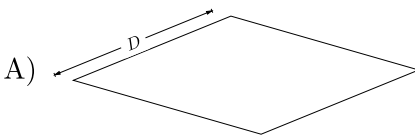
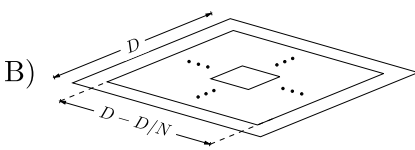
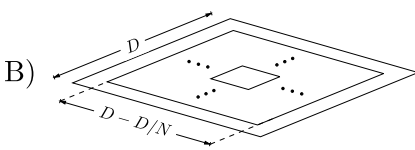
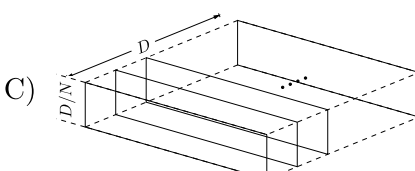
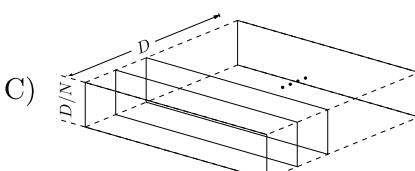
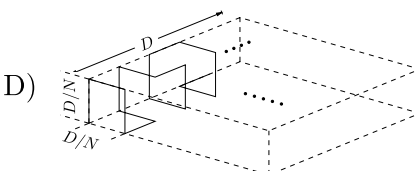
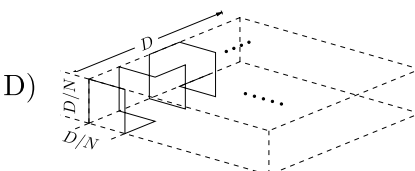
Eqs. (6), (9) and (10) are then used to find an expression for λ_f with d and I eliminated:

$$\lambda_f = \left(\frac{\mu^4 \rho_c^3 \rho_r^2 (1 + \alpha(\Gamma_e - \Gamma_r))^2}{16384 \cdot \pi \Gamma_e^8 \epsilon^2 \sigma_B^2 B_0^4 R_E^{12}} \right)^{\frac{1}{3}} \cdot \frac{D^{\frac{10}{3}} l}{A_e^{\frac{4}{3}}} \sigma_A^{\frac{1}{3}} \quad (11)$$

$$= C_1 G(N) D^{\frac{5}{3}} \sigma_A^{\frac{1}{3}}$$

where the constant C_1 is the bracketed term in Eq. (11), and $G(N) = (D^{\frac{5}{3}} l)/A_e^{\frac{4}{3}}$ is a factor determined by the coil geometry, where it is noted

Table 1
Current loop geometries.

Loop Geometry	Enclosed Area, A_e	Path Length, l
 <p>A) </p>	$A_e = D^2$	$l = 4D$
 <p>B) </p>	$A_e = \sum_{i=1}^N \left(\frac{i}{N} D \right)^2$ $= \frac{D^2(N+1)(2N+1)}{6N}$	$l = \sum_{i=1}^N 4 \frac{i}{N} D$ $= 2D(N+1)$
 <p>C) </p>	$A_e = \sum_{i=1}^{N+1} \frac{D^2}{N}$ $= \frac{D^2(N+1)}{N}$	$l = \sum_{i=1}^{N+1} \frac{2D}{N} + 2D$ $= \frac{2D}{N}(N+1)^2$
 <p>D) </p>	$A_e = N \sum_{i=1}^{N+1} \frac{3}{4} \left(\frac{D}{N} \right)^2$ $= \frac{3D^2(N+1)}{4N}$	$l = 4ND$

that the D term is eliminated for the geometries considered here in Table 1 leaving some function of the coil number N . This is the case for any geometry where the enclosed area A_e scales with D^2 while path length scales with D , which is true in general if both dimensions of the enclosed area scale with D .

Eq. (11) holds for geometries B, C and D in Table 1, so long as the number of coils/layers in the structure N is sufficiently large that the mass density of the structure can be assumed to be approximately uniform, as was assumed in Eq. (8). For geometry A, this assumption does not hold and the derivation must be modified to account for the uneven mass distribution of the single, outer current loop. The final expression for λ_f in this case is omitted here for brevity, but is derived by calculating the maximum gravity gradient torque for a body with inertia tensor components $i_1 = i_2 = (\frac{1}{12}(M - M_c) + \frac{4}{3}M_c)D^2$, and $i_3 = 2i_1$.

In summary, an expression for λ_f has been derived, which gives the fraction of the total mass that must be comprised by the conducting pathway in order to produce a torque as great as the maximum gravity gradient torque a planar spacecraft may experience, while maintaining a specified equilibrium temperature in the conducting path.

Plots of λ_f , d , I and P_j/D^2 are shown in Fig. 3 for geometry A, and Fig. 4 for geometries B-D. For geometries B-D the equations have the same form with different horizontal axis scaling since the $G(N)$ factor is unique to each geometry. It is assumed the conductor is a copper wire, and that the spacecraft is fabricated from some polycarbonate printed structure, so that the wire temperature should not exceed the glass temperature of 147 °C. Other physical data is summarised in Table 2. For geometry A it is noted that there are two branches for the solutions due to the uneven mass distribution. This is because at some length scales the gravity gradient torque can be counteracted either

by a lightweight current loop with a more massive structure, or by a more massive current loop capable of carrying a greater current. This more massive current loop is capable of carrying a greater current, thus producing a greater torque and offsetting the increase in inertia and thus greater gravity gradient torque. For the other coil geometries, the conductor mass is uniformly distributed and therefore this branching of the solutions does not appear. Fig. 3 shows that for a single, outer current loop, length scales on the order of 100 m to 1000 m could be feasible to meet the given criteria, for areal mass densities on the order of near to far term solar sails. The plot of the required areal power density is included, as it was assumed in the derivation that the available power would not be a limiting factor for this attitude control strategy. This assumption is likely valid, as the required areal power density is relatively insignificant when compared to the solar insolation of 1368 W/m² the spacecraft will intercept on-orbit, and PV panels covering a small fraction of the spacecraft surface will be capable of powering the system. Note that the red points on the plots represent the length scale at which $\lambda_f = 1$, and therefore solutions beyond (or below for that branch of the solution in the case of geometry A) are unphysical.

For geometry B, the length-scaling is found to be much more favourable than the outer loop geometry, with length scales on the order of 10 km meeting the criteria of the thermal and torque equilibrium equations. Both geometries C and D are seen to have much more adverse scaling than geometry B. As discussed previously, this is due to the fact that the area enclosed by these current loops relies on the structure having some depth, which will by definition be the smallest dimension of the planar structures considered here. For both cases, length scales on the order of 100 m would be feasible, and the

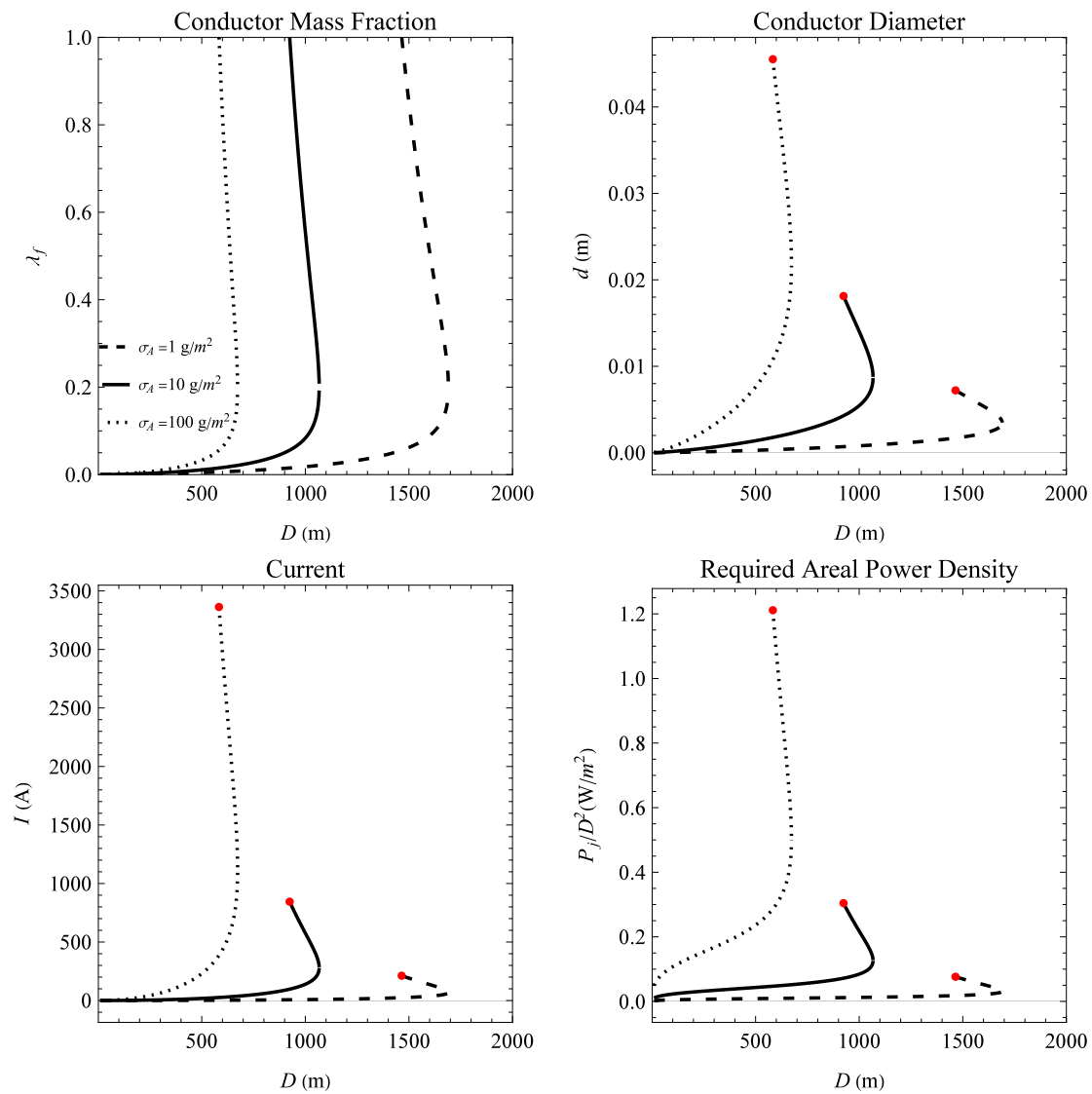


Fig. 3. Scaling for coil geometry A.

power requirements are also well within what could be considered reasonable for such structures. Figs. 3 and 4 both show the scaling functions for $N = 27$, i.e. for a structure with a depth dimension that is 3.7% its length. This value was chosen here as this is the value used in later simulations, where larger values would result in excessive computation times. For geometries B-D, the factor $G(N)$ influences the length-scaling however and must be considered. The change in the maximum length scale - i.e. the length scale at which $\lambda_f = 1$ (the top line of the λ_f plots in Figs. 3 and 4) with N is shown in 5. For geometry B, increasing N increases the number of current loops (which lie in the plane of the structure), and it is seen to increase the maximum possible length scale at which the torque from the current loops can equal the gravity gradient torque (i.e. the plot shows that having multiple, thinner current loops is more thermally efficient than fewer loops). Although the plot suggests that N could be increased indefinitely to achieve greater torques, there will be a practical limit on how thin a useable conductive wire can be which we do not consider here. For both geometries C and D, the maximum length scale decreases with N , as these geometries rely on the structure's depth which also decreases with increasing N , and so a greater number of current loops enclosing an ever-decreasing area is seen to be less mass-efficient in this case.

In the length-scaling analysis, radiative heating due to the wire being illuminated by the Sun was not included in the thermal model,

both for simplicity and as it was assumed the reflective membrane would be directed towards the Sun and thus shade the conductive wire. Given solar irradiance in LEO of 1360 W/m^2 , assuming that 70% of this is absorbed by the wire, ($\epsilon = 0.7$), which has an illuminated area of $A_s = l \times d$, the (worst-case) radiative heating power is $P_S 1360 * \epsilon * A_s = 952 \times ld \text{ (W)}$. The power dissipated through thermal radiation (Eq. (5)), for a wire temperature of $T_e = 420 \text{ K}$, is given by $P_r = 3880.2 \times ld$, or approximately $4P_S$. This addition to the thermal energy balance would require an increased wire diameter to maintain the required temperature, but as a 25% increase it is not the dominant contribution and does not significantly alter the length-scaling analysis here. In practice, this increase in wire diameter may be built in as a safety factor anyway, or another solution could be to reduce the current or implement pulse width modulation (PWM) when the current loop is illuminated. This would reduce the control effectiveness during illumination, but maintain the lower mass requirement of non-illuminated operation. A trade-off between these strategies could be performed, depending on the specific pointing requirements of the application considered and whether the wire will be shaded by the membrane during operation.

Results of analysis for all geometries show that the use of conductive pathways embedded in a large, planar structure could feasibly be used for attitude control purposes at length scales on the order of kilometers,

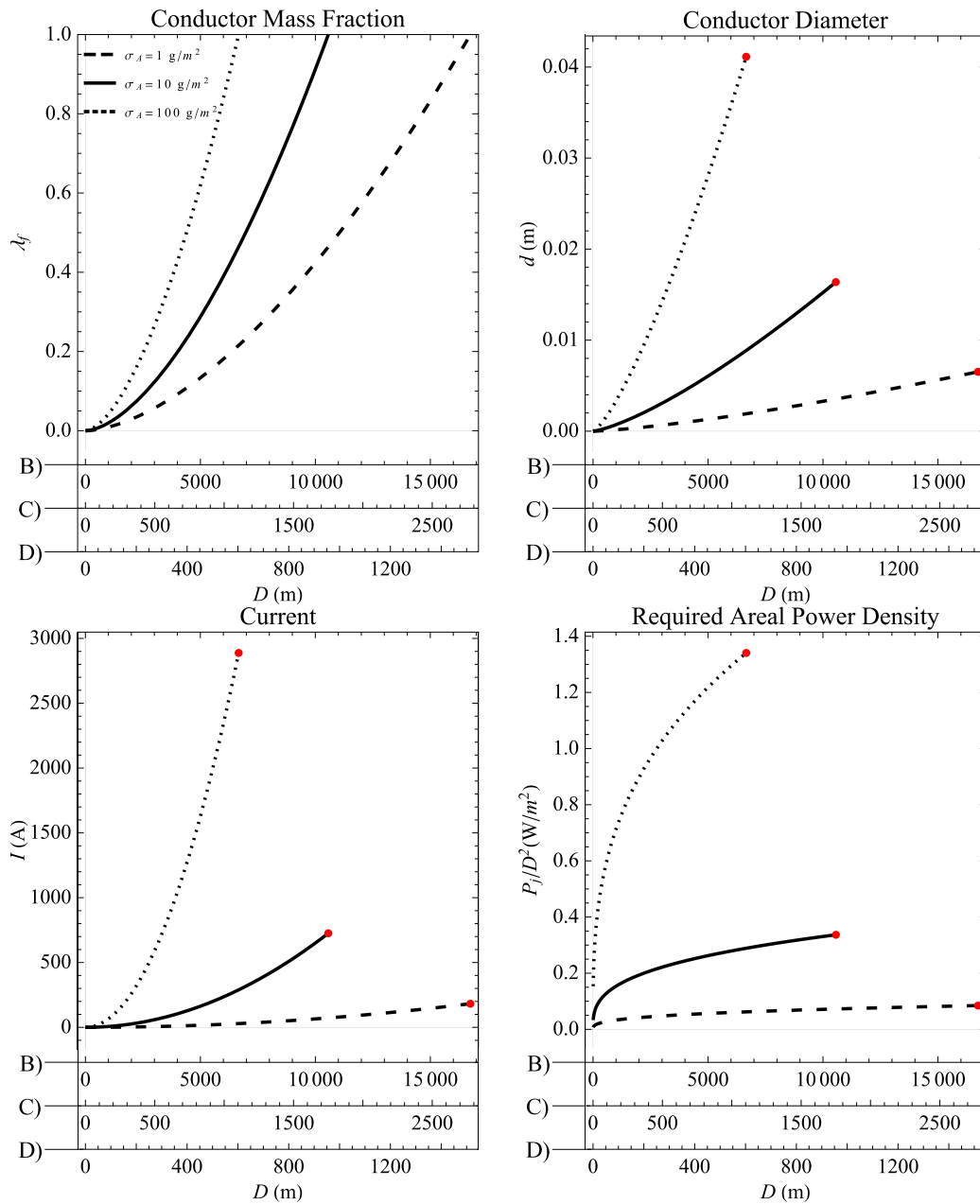


Fig. 4. Scaling for coil geometries B, C & D ($N = 27$).

though in practice this length scale is more likely to be reduced to the order of 100 m. This is due to the fact that large values of λ_f would not be physically realisable, as this would constitute the structure being comprised solely of the thin copper wire and leave no mass for the actual supporting structure. Furthermore, the analysis was performed for each coil geometry individually, while in practice it would most likely be required to have three, orthogonal current loop geometries overlaid with one another, such that three-axis magnetic control could be implemented. In other words, although analysis of geometry B has suggested length-scales on the order of 10 km may be feasible, the length-scale of the worst-performing geometry will be the limiting factor if three-axis control is desired. Though we have not analysed any other actuation forms here, it may be possible that geometry B could be employed for a kilometer scale structure, providing torque around one axis only, and then be supplemented by another form of attitude control such as an array of CMGs or the use of solar radiation pressure to enact torques around other axes.

4. Simulations of flexible structures with embedded current loops

Although it has been demonstrated that current loops can provide sufficiently large torques for attitude control purposes, a further consideration is whether they are capable of reorienting a highly flexible structure successfully. The structural response is particularly of interest for current loops because the torque produced by the current loop is the result of integrating the Lorentz forces on the current carrying wire around the loop. For a rigid current loop this produces a pure torque as described by Eq. (1), but for a flexible loop these forces act to deform the structure (effectively modifying the enclosed area). Additionally, this behaviour is highly nonlinear in that the direction of the forces acting on the current loop depends on the changing shape of the current loop/structure at a given point in time. The dynamics of flexible structures with embedded current loops are investigated in this section by performing numerical simulations of a 250×250 m square truss structure, for a range of structural flexibilities and N ,

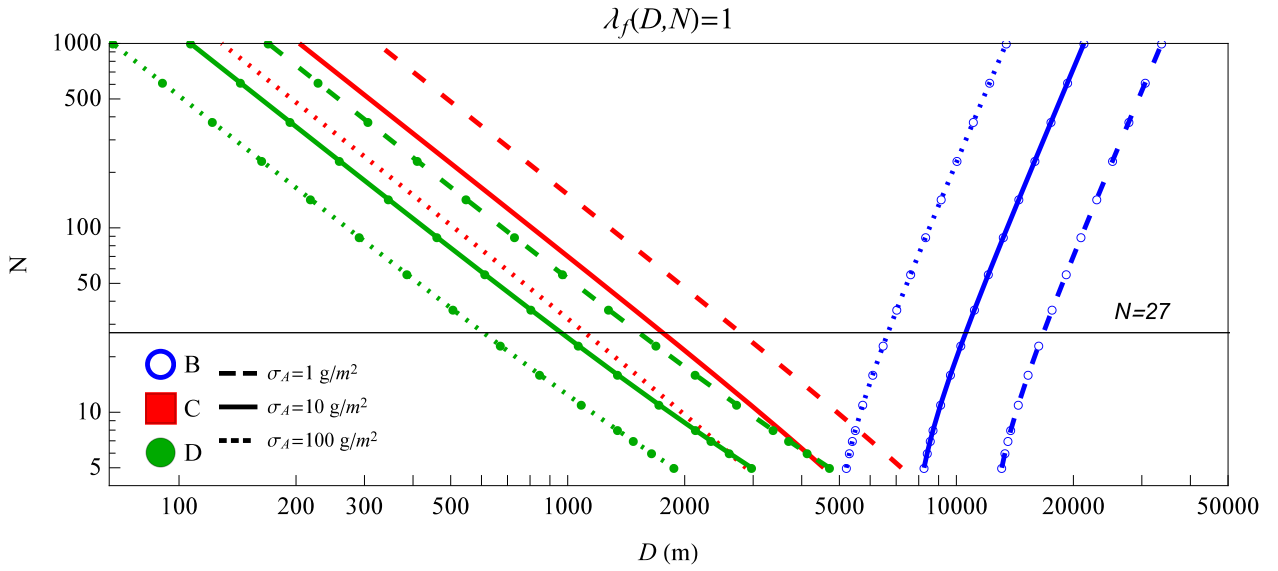


Fig. 5. Number of coils N against maximum length scale (D at which $\lambda_f = 1$) for uniform mass density coil geometries.

for each of the coil geometries presented in the previous section. The aim of these simulations is to determine how rigid a structure of this length-scale would need to be for this attitude control strategy to be considered feasible, and furthermore to gain some general insight into the nature of the structural deformations and dynamics observed in the structure when the current loops are energised. At this stage, gravity is not included in the model so that the structural deformations are entirely due to the current loop interacting with the magnetic field. Gravity forces are then included in Section 5, where attitude control using the current loops is demonstrated.

4.1. Model description

The structure is modelled as a spring–mass system (also commonly known as a lumped-parameter or multi-particle model [16]), following Ref. [2]. This gives a computationally efficient model of a general, flexible LSS. In this paper, the equations are recast in matrix form, as opposed to in Ref. [2] where the particle forces were determined iteratively. This reduces the computation time of the model and also allows a modification to the damping term detailed here. In matrix form, the equations are:

$$M\dot{r} = F^{\text{mag}} - K(r - R_\theta r_0) - \gamma \dot{r} \quad (12)$$

where M is the diagonal mass matrix, F^{mag} the Lorentz forces, K the stiffness matrix, r the particle positions, r_0 the equilibrium/initial particle positions (and R_θ the rotation matrix found by least-squares fitting a rotation between r_0 and r) and γ the damping matrix. As in Ref. [2], the system is comprised of point masses connected by linear springs, and so the stiffness matrix is assembled in the usual way (e.g. [17]). In terms of the adjacency matrix A defining the structural connectivity (defined in Ref. [2]), the stiffness matrix can be constructed from 3×3 submatrices according to:

$$K_{ij}^{3 \times 3} = \begin{cases} \sum_{i'=1}^{i-1} A_{i'j} + \sum_{j'=j}^{N_p} A_{ij'} \mathcal{K}^{ij'} & \text{if } i = j \\ -A_{ij} \mathcal{K}^{ij} & \text{otherwise} \end{cases} \quad (13)$$

where N_p is the number of particles, and \mathcal{K}^{ij} the first 3×3 submatrix of the global stiffness matrix of a 3D linear spring [17], given by:

$$\mathcal{K}^{ij} = k_{i,j} \begin{bmatrix} c_x^2 & c_x c_y & c_x c_z \\ c_x c_y & c_y^2 & c_y c_z \\ c_x c_z & c_y c_z & c_z^2 \end{bmatrix} \quad (14)$$

where $c_x = (x_j - x_i)/L_{i,j}$ is the cosine of the angle between the local and global x axes (with equivalent expressions for y and z),

and k_{ij} is the spring constant of the spring connecting particles i and j . This is determined by first selecting the desired overall beam-like bending stiffness EI of the structure, relating this to an equivalent beam element elastic modulus E and cross section A_c following Ref. [2] ($EI = 2EA_c R_c^2$), and setting $k_{i,j} = EA_c/L_{i,j}$, for $L_{i,j} = \sqrt{(x_j - x_i)^2 + (y_j - y_i)^2 + (z_j - z_i)^2}$ which is the natural length of the spring.

In Ref. [2] viscous damping with a uniform damping coefficient value for each spring element was used, with a value chosen that provided numerical stability without significantly affecting the response (i.e. near zero damping for all vibration modes). In this paper we instead use Caughey or modal damping to provide increased numerical stability and to give damping behaviour more closely representing that of an LSS in general, though of course the damping behaviour can vary greatly depending on the specific design and construction. The Caughey damping matrix is defined [18]:

$$\gamma = M \left(\sum_{n=1}^{N_\phi} 2\xi_n \omega_n \phi_n \phi_n^T \right) M \quad (15)$$

where M is the (diagonal) mass matrix, ξ_n the damping ratio, N_ϕ the total number of vibration modes, ω_n the modal frequency and ϕ_n the mode shape for the n th mode of the undamped system in all cases. The mode shapes and natural frequencies of the undamped system are found in the usual manner by solving the eigenvalue problem $|K - \omega^2 M| = 0$ (e.g. [19]). The damping ratios for each mode are then specified. For the first 100 modes, the damping ratio was set to 1% of critical damping. For all modes with mode number $n > 100$ the damping ratio is either equal to the Rayleigh (proportional) damping value, $\xi_n = 2\xi_{100}\omega_n/\omega_{100}$ or 10, whichever is greater, where $\xi_{100} = 0.01$ is the damping ratio of the 100th mode. These values are chosen in an attempt to represent a general LSS, which will most likely have very light damping of the low-frequency modes (under 10% without active vibration control [20]) while the high-frequency, more localised vibration modes would have higher damping. The damping ratio was given an upper limit of $\xi = 10$ as it was found that higher values led to numerical instability for the structural cases considered here.

The Lorentz forces acting on particle i of the spring–mass model due to the current carrying wires is determined by:

$$F_i^{\text{mag}} = \sum_{j \in C_L} \frac{1}{2} I_L r_{ij} \times B - \sum_{j \in C_L} \frac{1}{2} I_L r_{ij} \times B \quad (16)$$

Table 2
Simulation parameters.

Structural simulation parameters			Loop geometry:	A	B	C	D
Length	D	250 m	N	Current, I (Amps)			
Areal mass density	σ_A	100 g/m ²	12	42.60	15.28	35.64	47.53
Damping ratio	ξ_n	0.01 ($n < 99$)	19	42.60	10.02	36.68	48.91
Beam-like bending stiffness	EI	$10^3, 10^4, 10^5$ N m ²	27	42.60	7.457	37.24	49.65
Integration timestep (for EI)	dt	0.1, 0.05 , 0.01 s	Attitude control simulation parameters				
Integration method		4th order Runge–Kutta	Length	D	250 m		
Magnetic field strength	B	27.7 μ T (800 km)	Unit number	N	19		
Current loop physical data			Bending stiffness	EI	10^4 N m ²		
Density of copper wire	P	8960 kg/m ³	Loop Geometries	–	[C, C, B]		
Reference temperature	T_r	293 K	Max. currents	\vec{I}^{max}	[36.68, 36.68, 5.644]		
equilibrium temperature	T_e	420 K	Max. dip. moment	m^{max}	2.413×10^6 A m ²		
Reference resistivity at T_r	ρ_r	1.68×10^{-8} Ω m	Control gains	k_p	600		
Grey-body emissivity	ϵ	0.7		k_ω	4×10^5		
Temperature coefficient	α	0.00404 K ⁻¹	Orbital altitude	R_o	800 km		
Stefan–Boltzmann constant	σ_B	5.67×10^{-8} W m ⁻² K ⁻⁴	Integration timestep	dt	0.05 s		
Magnetic field (sea-level)	B_0	3.12×10^{-5} T	Simulation runtime		10 000 s		
Std. gravitational parameter	μ	3.986×10^{14} m ³ s ⁻²	Mag. field model		WMM (2022) [21]		
Mean radius of Earth	r_e	6370 km	(Other data same as structural simulations.)				

where $C_L = \{j|A_{ij}^L = 1\}$ and $C_L^- = \{j|A_{ji}^L = 1\}$ are the sets of particle indices where a current carrying element of loop L is connecting particles i and j , with current flowing from i to j or from j to i respectively. The current loops are defined by the directional adjacency matrix A^L , in which $A_{ij}^L = 1$ if a current carrying element connects particles i and j with current flowing in that direction. The adjacency matrices define the direction of “positive” current, and the same matrix then gives the correct forces for current flowing in the opposite direction if the loop current I_L takes a negative value. The “positive” current direction is defined for the current loop geometries here such that the magnetic dipole moment of the current loop points in the positive xyz direction for the geometries shown in Fig. 1 (i.e. the current loops all follow the right hand rule, winding anti-clockwise around their respective axis). Each current loop geometry has a unique adjacency matrix, which is computed prior to the simulation being performed. The overall magnetic force vector F^{mag} is then found by summation over all current loops (if multiple loops are defined/present) and assembling the particle force vectors into a single vector for use in Eq. (12). Note that we only consider forces due to interaction with the external geomagnetic field, and not any interaction with the magnetic field generated by the current loops themselves. This assumption is made because it was found that the magnetic field strength generated by the current loop, measured at some other perpendicular point of the loop, would be much lower than the geomagnetic field strength and thus would not be a significant contribution to the particle forces. The magnetic field generated by a straight, current carrying wire is given by:

$$B_w = \frac{\mu_0 I}{2\pi r} \tag{17}$$

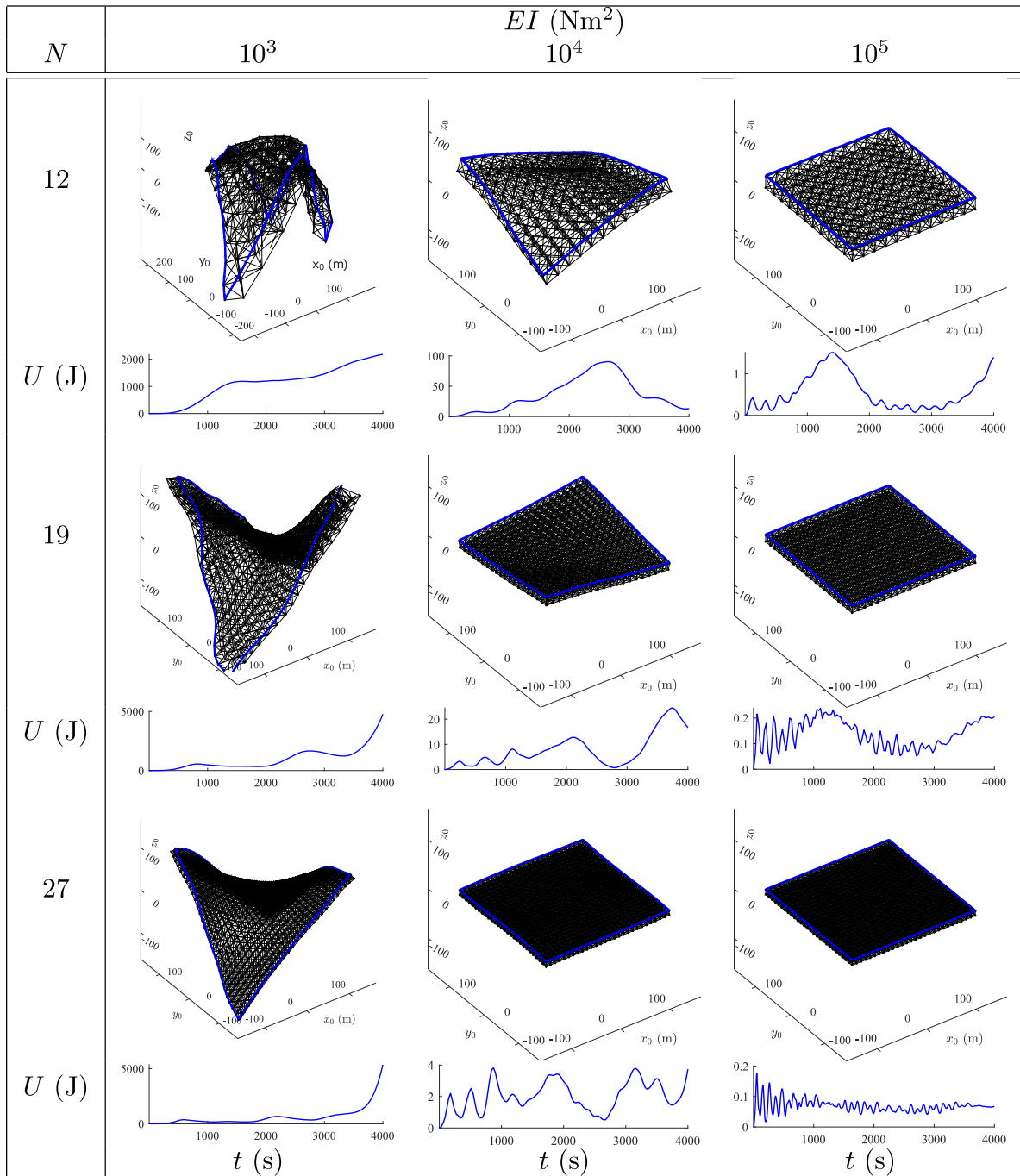
where $\mu_0 = 4\pi \times 10^{-7}$ H/m is the magnetic permeability of free space, and r the distance from the wire. For the cases considered in the following simulations, the current is on the order of 10 A, and the structural unit spacing (and thus closest spacing between parallel wire elements) is on the order of 10 m, resulting in the self-interaction field being on the order of 10^{-7} T, two orders of magnitude lower than the geomagnetic field in LEO. The self-forces due to the current loop’s own magnetic field are therefore assumed to be negligible for the cases considered in the following simulations. For a tightly packed structure (<1 m unit spacing) with loop currents > 100 A, the field generated by the current loop could be comparable to the geomagnetic field and act to compress/expand the units of the structure, and would need to be considered in the analysis.

4.2. Simulation results

Using the spring–mass model, simulations have been performed for each of the current loop geometries A–D shown in Table 1. As noted, the aim of these simulations is to determine how rigid the structure must be to withstand the forces acting on the current loop and be gently rotated, when that current loop is capable of producing a torque at least as large as the maximum gravity gradient torque the structure would experience. Simulations are performed for each of the four loop geometries, and for three values of both the equivalent bending stiffness EI and the number of structural units N . Varying N changes both the number of current loops for geometries B–D, and the structural depth. There are therefore nine simulations performed for each of the four geometries, resulting in 36 simulations total. Each simulation is performed in free-space with a fixed external magnetic field direction with no other disturbing forces considered. This choice is made so that the deformation of the structure under application of the Lorentz forces can be directly observed and compared for each case without other factors affecting the structural dynamics. In all cases the structure is initially at rest, and the magnetic dipole moment is perpendicular to the magnetic field. The loop has a constant current, and then Eq. (12) is numerically integrated for 4000 s. Under these conditions, a rigid current loop would undergo simple harmonic motion, completing a rotation of 180 deg and then reversing direction. The simulation parameters are summarised in Table 2, where the loop currents are calculated following the derivations in Section 3. A length scale of 250 m is selected as this results in a λ_f value of <10% in all cases (following Figs. 3 and 4), which we consider to be an upper limit on a reasonable mass allowance for the attitude control system of a gossamer structure of this size. Following Ref. [2], 10^3 N m² is taken as a reference beam like bending stiffness for a solar sail-type gossamer spacecraft, and we then consider two orders of magnitude greater to cover a wide range of structural flexibilities. The areal mass density is selected as 100 g/m² by considering that near term solar sails can have an areal mass density on the order of 10 g/m², and thus an order of magnitude greater than this is thought to be a reasonable value to cover the range of flexibilities we consider here. The magnetic field strength is considered a typical value for an orbital altitude of 800 km, determined by Eq. (7). The values of N were chosen to cover a range of values, with an upper limit of 27 selected due to exceedingly long computation times for values greater than this.

Results of the simulations are shown in Tables 3 and 4. The figures show the structure at the point of maximum strain energy (shown in the x_o, y_o, z_o body frame), and a plot of strain against time throughout

Table 3
Results of simulation for Geometry A.

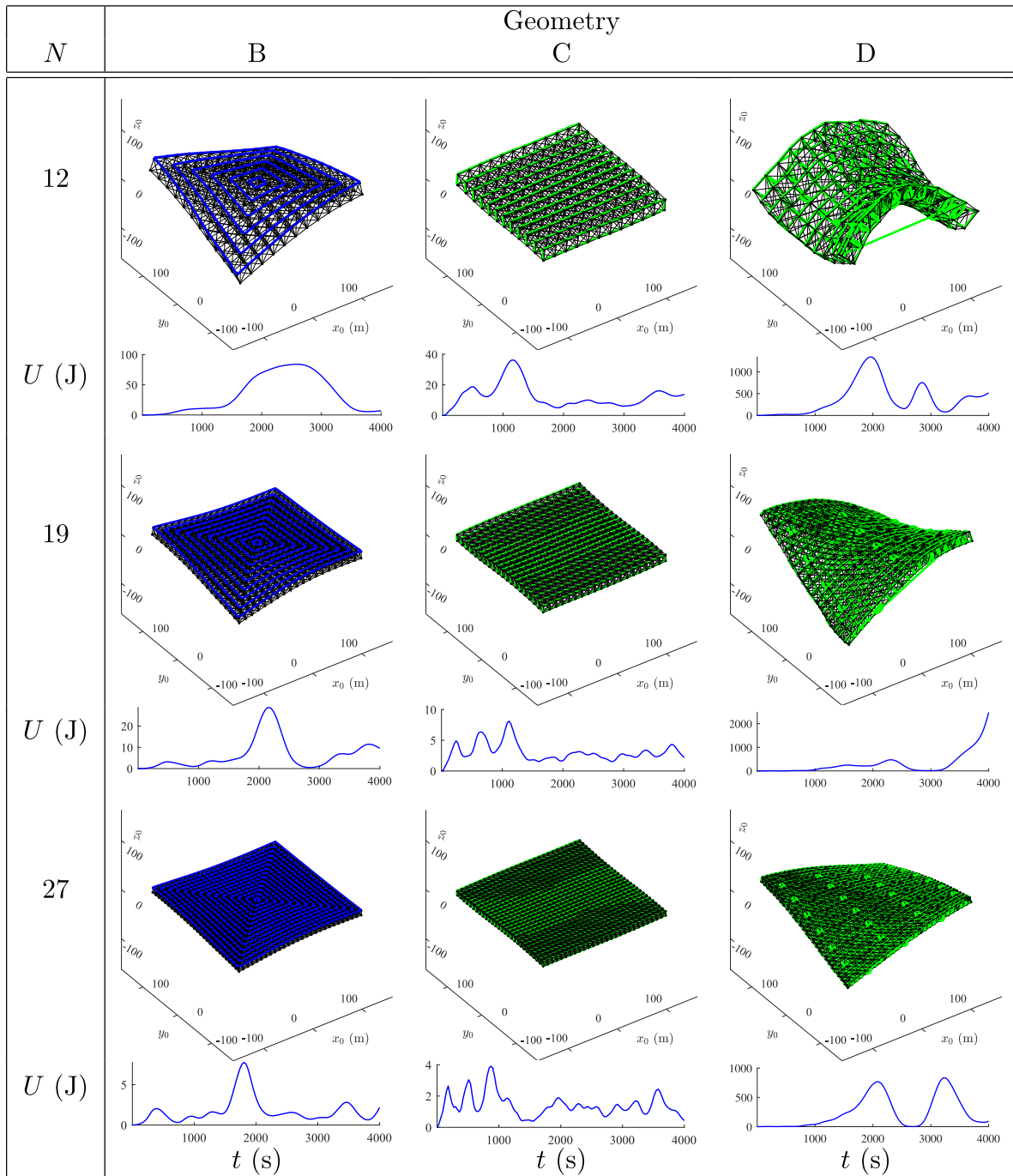


the simulation. The total strain energy U is calculated by summation of the contribution of each spring element in the model, where the spring potential is $1/2k_{ij}L_{ij}^2$, where k_{ij} and L_{ij} are the spring constant and extension respectively of the spring element connecting particles i and j . The x_0, y_0, z_0 body frame is initially aligned with the xyz inertial frame as shown in Fig. 1. The structure itself is drawn in black while the current loops are coloured blue and green for the z and y direction dipole moment loops respectively. Table 3 shows plots for all nine simulations performed for geometry A, while results for the other geometries are only shown for $EI = 10^4$ N m². In all cases, it was found that a bending stiffness $EI = 10^3$ N m² was too flexible for the current loop to rotate successfully, and the structure would collapse (as in the first column of Table 3). In particular, for

geometries C and D, the orientation of the magnetic field and resultant Lorentz forces ended up stretching the structure in the z direction, to a distance of over 500 m. Although the structure essentially folds up in these simulations, it is important to note that this model does not exactly represent a membrane, in that the springs here are linear and behave the same under tension and compression. This represents a general, homogeneous flexible truss structure rather than a gossamer spacecraft specifically. For a gossamer spacecraft of this flexibility, it is likely that the tensioning of the membrane would be a significant contribution to the structural response. Although it was thought that an electromagnetic current loop could in fact be used to tension the membrane of such a spacecraft, our results suggest that this would not be possible in practice. This is because, although some of the forces on

Table 4

Results of simulation for Geometries B, C and D ($EI = 10^4 \text{ N m}^2$), z_0 direction dipole moment loops (A) are shown in blue while y_0 direction loops (C,D) are shown in green.



the current loop would act to tension the membrane in one direction, there are always force pairs that will act to collapse/fold the structure in a direction perpendicular to these forces. In the simulation results this was observed most clearly for geometries C and D, as the structure was stretched in the z direction, and simultaneously compressed in the x direction. However, we note that this result is due to the interaction of the current loop with the external, geomagnetic field. For much higher currents, requiring superconducting loops, it has been demonstrated [10–12] that tensioning could be achieved via the self-forces in the wire. For $EI = 10^5 \text{ N m}^2$, it was found that the structure behaves essentially as a rigid body in all cases, and thus for structures of this

rigidity large current loops would be an effective means of attitude control, and standard rigid-body control laws may be used.

The chosen current loop geometries all resulted in quite different structural responses. This is because although the torque in all cases is the same, the forces which result in that torque have different magnitudes and are applied at different points. Comparing the z direction loops (A and B), the structural deformation and maximum value of the total strain are quite similar in each case, though there is some difference in the strain profiles for $N = 19$ and 27 . For geometry B, there is a large peak in U at approximately 2000 s, whereas for geometry A there are larger oscillations in U over the entire simulation. At 2000 s the magnetic dipole moment is aligned with the field direction, and

this is the point of minimum torque, but maximum “stretching” of the structure (as discussed in the previous paragraph). This suggests that although there is a slight benefit to having multiple planar current loops in that the structure can be more smoothly rotated, the tensioning of the current loop/s at certain orientations results in similar deformations for both cases. Comparison of geometries C and D shows that for achieving a magnetic dipole moment in this direction, geometry C performs much better than the coil type geometry, with the strain energy two to three orders of magnitudes lower for the cases here. This is because for geometry D, there are many more opposing force pairs present which act to deform the structure instead of producing the desired torque, and these force pairs are always located in the same unit of the structure, whereas for C these forces act at opposite ends of the structure (the vertical loop elements at the edge of the structure). Considering the variation of N for cases B and C, there is a clear benefit to having a greater number of current loops in that the total strain is greatly reduced and the rotation is more similar to that of a rigid body.

Overall the results show that current loops are capable of smoothly rotating flexible structures, though for a given areal mass density there will be a minimum level of structural rigidity required to prevent excessive stretching of the structure. For a 100 g/m^2 structure results suggest a beamlike bending stiffness of approximately 10^4 N m^2 is sufficient. Although the current loops failed to rotate more flexible structures in this case, it is important to note that more flexible structures may have a lower mass than that considered here, and thus the torque applied in these simulations may be greater than would be required for their attitude control, though our analysis is restricted to 100 g/m^2 here. In all cases, having a greater number of current loops which distribute the Lorentz forces more evenly across the structure was found to result in lower structural deformation.

5. Attitude control simulation of a conductive structure

Having found that embedded current loops are capable of rotating a flexible spacecraft, this section now demonstrates the attitude control of a large space structure using current loops, in the presence of gravity gradient torques and a representative magnetic field model. A 250 m square planar structure is again considered, with multiple embedded current loops allowing three axes of controllable magnetic dipole moment. Current loop geometries B and C are considered, such that the structure is composed of a square lattice containing loop geometry B and two perpendicular cases of geometry C overlapping in the same structure. The spacecraft is placed in an 800 km altitude, circular polar orbit. An areal mass density of 100 g/m^2 and beam-like bending stiffness of $EI = 10^4 \text{ N m}^2$ is selected, in keeping with the previous section where it was determined such a structure may be successfully rotated by embedded current loops with relatively little structural deformation. The spacecraft structural model is the same as in the previous section, as given by Eq. (12). Gravitational forces are now added to Eq. (12), which are calculated for each point-mass particle of the model (using $F_i^{grav} = (\mu m_i / |\mathbf{R}_i|^2) \hat{\mathbf{R}}_i$, where \mathbf{R}_i is the position vector of particle i in an Earth centred inertial frame). As noted, gravity forces were not included in the analysis of Section 4, as the aim of these simulations was to investigate the structural deformation and rotations caused by the conductive current loops. Now gravity is introduced to demonstrate that the current loops could be used for attitude control purposes in LEO, where gravity will be a disturbing force. As the gravitational force on each particle is calculated individually using that particle’s position, variations across the structure naturally lead to gravity-gradient torques in the simulation. The structure is placed onto the desired orbit by giving every particle an initial velocity in the z -direction equal to the orbital velocity $v_o = \sqrt{\mu/R_o}$. The magnetic field is now calculated at each timestep of the simulation by determining the position of the structure’s centre of mass in an Earth-centred inertial frame and finding the value of the World Magnetic Model (WMM) at that position [21]. It is assumed that there is no variation of the field across the structure

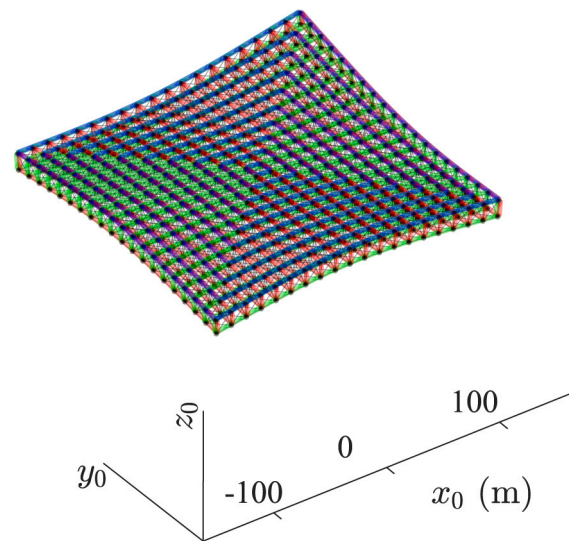


Fig. 6. Structural displacement at maximum strain ($t = 9339 \text{ s}$).

to avoid evaluating the WMM multiple times and save computation time. In all other respects the simulation and model are the same as the previous section.

A proportional-derivative (PD) type quaternion error feedback control law is implemented, which is commonly used for magnetic attitude control [22]. The controller generates reference control torques according to:

$$T_{ref} = -k_p q_{err} - k_\omega \omega \tag{18}$$

where q_{err} is the vector part of a quaternion representing the rotation between the current attitude and the desired attitude, ω is the body rate vector, and k_p and k_ω are the control gains. Once a reference torque is found, the magnetic dipole moment necessary to generate this torque is then given by:

$$\mathbf{m}_d = \frac{\mathbf{B} \times T_{ref}}{|\mathbf{B}|} \tag{19}$$

from which the loop currents are determined, according to:

$$\mathbf{I} = \left(\frac{\mathbf{m}_d}{m^{max}} \right) \cdot \mathbf{I}^{max} \tag{20}$$

$$I_L = \text{sign}(I_L) I_L^{max} \quad \text{if } I_L > I_L^{max}$$

where \mathbf{I}^{max} is the vector of maximum allowable currents in the loops calculated from Eq. (9), and m^{max} is the magnitude of the magnetic dipole moment of each loop at maximum current (which is the same value for all loops). The current vector \mathbf{I} has components I_L , with $L = x, y, z$ corresponding to current in the xyz direction dipole loops respectively. The second line of Eq. (20) ensures that the current in each loop does not exceed the maximum allowable value. The control gains are selected following a trial-and-error approach, using a rigid-body simulation (which is faster to evaluate compared to the spring-mass model) with an equivalent inertia tensor to the spring-mass model. The structure is initially lying in the xy plane, and the desired rotation is a 90° slew manoeuvre around the y -axis. Simulation data and model parameters are summarised in Table 2.

5.1. Results of simulation

Simulation results are shown in Fig. 7. The simulation was performed for $10\,000 \text{ s}$, which is approximately 1.5 orbits. The structure is seen to smoothly rotate, reaching the target attitude in 3000 s . As the structure orbits, it is then periodically disturbed by the gravity gradient torque, which results in attitude errors of up to 18° (at 6500 s), which

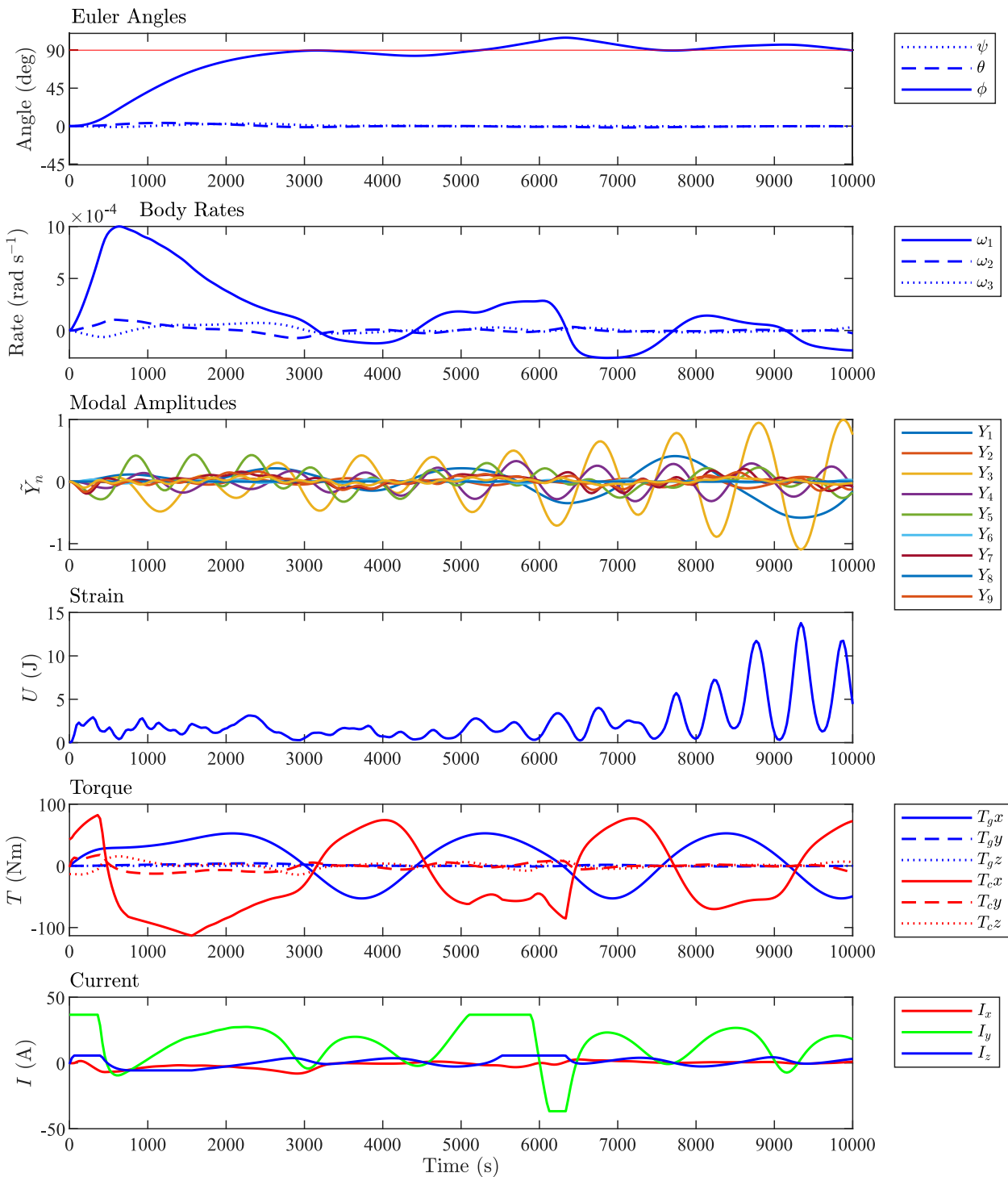


Fig. 7. Attitude control simulation results. (For interpretation of the references to colour in this figure legend, the reader is referred to the web version of this article.)

are then corrected by the controller. The torque profile shows that the actuation torque (blue) is mostly able to negate the gravity gradient torque (red), although at 5000 s there is a point where the controller is saturated, which leads to the large attitude error a short time later. The strain energy is calculated as in Section 4, while the normalised modal amplitudes are found by expressing the structure displacements as a superposition of the mode shapes in the standard way [17], and dividing by the maximum modal amplitude. The plots of strain energy and modal amplitudes show that the structural deformation is fairly small while the structure rotates, though there is some growing vibration of primarily the first and third mode shape towards the end of

the simulation. Fig. 6 shows a plot of the structure at 9339 s, the point of maximum strain energy in the system, showing that the structure is visibly deformed, though it is unlikely a displacement of this amplitude would cause failure due to buckling. While there are some growing vibrations towards the end of the simulation, these are to be expected due to the time-varying actuator and gravity forces. With some form of active or passive vibration control a damping ratio of closer to 10% of critical damping is expected to be a reasonable value for structures of this type [20], which would likely be sufficient to suppress these excitations on a longer timescale. The modal amplitudes show that the structure's deformation is made up of primarily the low frequency mode

shapes, which correspond to global deformation/curvature rather than local vibrations. This shows that the force pairs which occur within the individual units of the structure are evenly distributed and do not result in large deformation of the structural units or localised vibrations, which could be more likely to lead to structural failure, or failure of the wire or membrane attachment points. We also note that although there is some control saturation, this could be avoided by increasing the wire mass. The current loops here were sized to produce a maximum torque equal to the maximum possible gravity gradient, but this maximum can only be achieved when the loop is oriented perpendicular to the magnetic field. Therefore, it is likely necessary that in practice the current loops should be sized to produce a maximum torque slightly greater than the maximum gravity gradient torque to avoid the control saturation which occurred in this simulation.

6. Conclusion

Results of a length-scaling analysis and a simple thermal model show that embedded current loops should be considered as a viable form of attitude control for large space structures, particularly for lightweight, planar structures which are most likely to be realised by on-orbit manufacturing techniques in the coming years. The analysis suggests that current loops lying in the plane of the structure are capable of producing torques at least as large as the maximum gravity gradient torque for structures on the order of 1000 m in length, when a modest portion (<10%) of the total structural mass is afforded to the conductive material. To achieve 3-axis magnetic attitude control, some structural depth is required, and the length-scaling is found to be more adverse, though it seems feasible that this could be achieved for structures of lengths on the order of 100 m, again assuming <10% of the mass for the conductive loops and that the structures depth is at least 3% of the length.

Considering structural flexibility, results of simulation have shown that a 250 m square structure, with areal mass density of 100 g/m², would require a beam-like bending stiffness of at least 10⁴ N m² in order to not completely collapse under the effect of the Lorentz forces acting on the current loop. However, we note that a more flexible structure of lower mass would require lower torques to control, and it is possible current loops could still be viable in this case. Although it is possible that membrane tensioning via current loops could be possible, our results do suggest that any tensioning effect using current loops occurs simultaneously with a perpendicular compression of the structure, and so it appears unlikely that conductive loops interacting with the geomagnetic field could be used for this purpose. Simulations have shown that all the current loop geometries considered here are capable of rotating a flexible structure, though the structural deformation observed varies. In particular it was found that for current loops which enclose area in the depth dimension of a planar structure, having multiple large current loops is much preferred to having the coil type conducting pathway which was originally proposed in this paper.

Finally, an attitude control simulation has demonstrated that the strategy is capable of performing a slew manoeuvre and maintaining a set attitude, in the presence of gravity gradient torques and a representative magnetic field model. Overall, it is concluded that embedded current loops or conductive structures appear to be a promising form of attitude control strategy for large, lightweight space structures, and that the strategy is particularly appealing for the type of structure that may be 3D-printed on-orbit, due to the simplicity of the design and relative ease with which production of the large current loops could be integrated with the 3D-printing process.

Declaration of competing interest

The authors declare that they have no known competing financial interests or personal relationships that could have appeared to influence the work reported in this paper.

Acknowledgements

This work was supported by the Royal Academy of Engineering, UK under the Chair in Emerging Technologies scheme. CM was also supported by a Royal Society Wolfson Research Merit Award, UK.

References

- [1] E. Silani, M. Lovera, Magnetic spacecraft attitude control: A survey and some new results, *Control Eng. Pract.* 13 (3) (2005) 357–371, <http://dx.doi.org/10.1016/j.conengprac.2003.12.017>.
- [2] B. Robb, M. McRobb, G. Baile, J. Beeley, C.R. McInnes, Distributed magnetic attitude control for large space structures, *Acta Astronautica* 198 (2022) 587–605, <http://dx.doi.org/10.1016/j.actaastro.2022.06.045>.
- [3] W.M.J. Robbins, *The Feasibility of an Orbiting 1500-Meter Radiotelescope*, Tech. Rep. NASA CR-792, 1967.
- [4] Y. Yamada, T. Inamori, Y. Satou, T. Kawai, Y. Sugawara, Electromagnetic deployment of a membrane structure in LEO, *Jpn. Soc. Aeronaut. Space Sci.* 69 (5) (2021) 187–196, <http://dx.doi.org/10.2322/jssass.69.187>.
- [5] M.Y. Ovchinnikov, D.S. Roldugin, Progress in aerospace sciences a survey on active magnetic attitude control algorithms for small satellites, *Prog. Aerosp. Sci.* (May) (2019) 100546, <http://dx.doi.org/10.1016/j.paerosci.2019.05.006>, 0–1.
- [6] M. McRobb, B. Robb, S. Ridley, C. McInnes, Emerging space technologies: Macro-scale on orbit manufacturing, in: *17th Reinventing Space Conference, British Interplanetary Society, Belfast, Northern Ireland, 2019*.
- [7] R.P. Hoyt, J. Cushing, J. Slostad, G. Jimmerson, TrUSSelator: On-orbit fabrication of high-performance composite truss structures, in: *AIAA SPACE 2014 Conference and Exposition*, no. August, 2014, pp. 1–10, <http://dx.doi.org/10.2514/6.2014-4337>, URL <http://arc.aiaa.org/doi/10.2514/6.2014-4337>.
- [8] Y. Yamada, T. Inamori, J.H. Park, Y. Satou, Y. Sugawara, K. Yamaguchi, Attitude control of spin-type space membrane structures using electromagnetic force in earth orbit, *Adv. Space Res.* (ISSN: 0273-1177) 69 (10) (2022) 3864–3879, <http://dx.doi.org/10.1016/j.asr.2022.02.050>.
- [9] T. Inamori, T. Kawai, Y. Sugawara, Y. Sato, Attitude control system of a space membrane using electromagnetic torque, in: *The Proceedings of the Asian Conference on Multibody Dynamics*, Vol. 2016.8, 2016, http://dx.doi.org/10.1299/jsmeacmd.2016.8.09_1256733, (0).
- [10] V.Y. Kezerashvili, R.Y. Kezerashvili, Solar sail with superconducting circular current-carrying wire, *Adv. Space Res.* 69 (1) (2022) 664–676, <http://dx.doi.org/10.1016/j.asr.2021.10.052>.
- [11] G.V. Gettliffe, N.K. Inamdar, R. Masterson, D.W. Miller, High-Temperature Superconductors as Electromagnetic Deployment and Support Structures in Spacecraft, Tech. Rep. July, Massachusetts Institute of Technology, 2012, pp. 1–19.
- [12] G.V. Gettliffe, *Stability Analysis of Electromagnetically Supported Large Space Structures* (Ph.D. thesis), Massachusetts Institute of Technology, 2016.
- [13] I.D. Boyd, R.S. Buenconsejo, D. Piskorz, B. Lal, K.W. Crane, E. De La Rosa Blanco, *On-Orbit Manufacturing and Assembly of Spacecraft*, Tech. Rep., IDA Science and Technology Policy Institute, 2017.
- [14] M. Walt, The geomagnetic field, in: *Cambridge Atmospheric and Space Science Series*, Cambridge University Press, 1994, pp. 25–35, <http://dx.doi.org/10.1017/CBO9780511524981.007>.
- [15] M.J. Sidi, *Spacecraft Dynamics and Control: A Practical Engineering Approach*, Cambridge University Press, Cambridge, 1997, <http://dx.doi.org/10.1017/CBO9780511815652>.
- [16] Y. Shirasawa, O. Mori, Y. Miyazaki, H. Sakamoto, M. Hasome, N. Okuizumi, H. Sawada, H. Furuya, S. Matsunaga, M. Natori, J. Kawaguchi, Analysis of membrane dynamics using multi-particle model for solar sail demonstrator “IKAROS”, in: *Collection of Technical Papers - AIAA/ASME/ASCE/AHS/ASC Structures, Structural Dynamics and Materials Conference* (April), 2011, pp. 3–4, <http://dx.doi.org/10.2514/6.2011-1890>.
- [17] W. McGuire, R.H. Gallagher, R.D. Ziemian, *Matrix Structural Analysis*, second ed., Faculty Books, 2000, pp. 93–98.
- [18] J.L. Humar, *Dynamics of Structures*, third ed., CRC Press, 2002, pp. 512–514.
- [19] R.W. Clough, J. Penzien, *Dynamics of Structures*, 3, Computers & Structures, Inc., 2002.
- [20] M.S. Lake, L.D. Peterson, M.B. Levine, Rationale for defining structural requirements for large space telescopes, *J. Spacecr. Rockets* 39 (5) (2002) 674–681, <http://dx.doi.org/10.2514/2.3889>.
- [21] B.M. Chulliat, A., W. Brown, P. Alken, C. Beggan, M. Nair, G. Cox, A. Woods, S. Macmillan, M. Panizza, The US / UK World Magnetic Model for 2020–2025, Tech. Rep., 2020, <http://dx.doi.org/10.25923/ytk1-yx35>.
- [22] M. Lovera, A. Astolfi, Spacecraft attitude control using magnetic actuators, *Automatica* 40 (8) (2004) 1405–1414, <http://dx.doi.org/10.1016/j.automatica.2004.02.022>.